Summary of 5000 words for Ph.D. Pre-Submission Seminar

Name: **Santanu Roy**
Enrolment No.: **PU/PHD/PHYS/2018/015**
Registration No.: **R-18RS09160151**
Department of Physics, Presidency University, Kolkata
Name of the Supervisor: **Prof. Barun Raychaudhuri**
Department of Physics, Presidency University, Kolkata

Title: Assessment of atmospheric carbon dioxide and aerosols from ground spectroradiometry and hyperspectral image analysis

ABSTRACT

Monitoring of atmospheric greenhouse gases, such as carbon dioxide (CO_2), and of man-made aerosols have been subjects of global importance during the last few decades. This research work has carried out studies on the retrieval of atmospheric CO_2 and aerosols based on data derived from airborne and satellite-borne hyperspectral images validated with field spectroscopy. The spatial distributions of CO_2 abundance at tropical urban atmosphere of India are estimated using the hyperspectral images of Airborne Visible/Infrared Imaging Spectrometer Next Generation (AVIRIS-NG). The spectral bands of CO_2 absorption, as detected by AVIRIS-NG in such atmosphere are validated with hyperspectral field spectroradiometry, which account for atmospheric scattering, surface reflectance and variation of solar elevation. An image analysis technique, named *a*-DOAS has been developed for CO_2 assessment based on weighted averaging of the reflectance of absorbing and non-absorbing bands that minimized the wavelength dependence of surface reflectance. Also, a correction technique is put forward for water vapor absorption. The temporal variation of column averaged dry air CO_2 mole fraction in India and at global level obtained from NASA's recent-most sensor Orbiting Carbon Observatory-3 is analyzed and a wavelet coherence technique is suggested for quantifying the temporary reduction of CO_2. A technique for assessing the spatial distribution of aerosol effect at different places under the same atmospheric condition is put forward using the oxygen absorption (O2-A) band around 760 nm.

1. New Methodology for Optical Depth from Hyperspectral Data

Following the theory of differential optical absorption spectroscopy (DOAS), the extent of radiation absorption by the atmospheric gases can be expressed by the absorption depth (τ) given by

$$\tau = ln[\, L_0(\lambda)/L_a(\lambda)] = \sigma(\lambda)cl \quad (1)$$

In Eq. (1), L_0 and L_a are the radiances at wavelength λ before entering the atmosphere and after traversing the optical path (l). The concentration (c) and the narrowband component of the absorption cross-section ($\sigma(\lambda)$) of the gas species are supposed to be constant for a certain path length.

Fig. 1 presents some samples ground-measured radiance spectra for a typical urban site and compares the same with the spectra derived from AVIRIS-NG image. Two consecutive

CO_2 absorption bands, henceforth named CO_2-1 and CO_2-2, respectively, are noted on both the spectra. In the AVIRIS-NG spectra, more than one channels contribute in the CO_2 absorption band. To account for this phenomenon, the radiances of the channels are averaged (hence the term "*a*-DOAS") in order to incorporate their combined effect at the absorbing wavelength λ. Eqs. (2) and (3) express these two CO_2 absorption depths in terms of the weighted average of the radiance values at absorbing and non-absorbing wavebands.

$$\tau_{CO2-1} = \ln\left[\frac{\left\{\frac{L_{322}+L_{323}+L_{324}+L_{332}+L_{333}+L_{334}}{6.0}\right\}}{\left\{\frac{L_{327}+L_{328}}{2.0}\right\}}\right] \quad (2)$$

and

$$\tau_{CO2-2} = \ln\left[\frac{\left\{\frac{L_{332}+L_{333}+L_{334}+L_{341}+L_{342}+L_{343}}{6.0}\right\}}{\left\{\frac{L_{336}+L_{337}+L_{338}+L_{339}}{4.0}\right\}}\right] \quad (3)$$

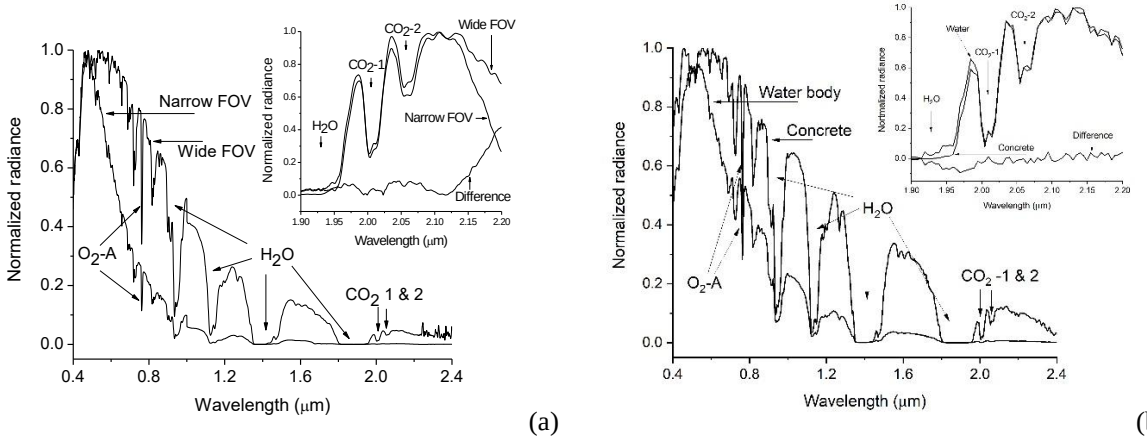

(a) (b)

Fig. 1. (a) Ground-based solar radiance spectra at a typical urban site measured with ASD spectroradiometer for narrow and wide angle FOV, the inset showing the enlarged view around CO_2 absorption bands (1 & 2). The water vapor (H_2O) and oxygen (O_2-A) absorption bands are also indicated. (b) Similar spectra derived from AVIRIS-NG image from pixels containing waterbody and concrete.

In order to minimize the surface reflection effect, the radiance values were normalized [Eq. (4)] for all pixels within the waveband range containing the CO_2 bands (band-315 or 1.9492μm to band-346 or 2.1044μm)

$$L_{i(norm)} = (L_i - L_{min})/(L_{max} - L_{min}) \quad (4)$$

where L_{min} and L_{max} represent the radiance value at band-315 and band-346, respectively. The $L_{i(norm)}$ values for the required bands were used in Eq. (2) and (3). Fig. 2 presents a comparative view of the variation of the reflected radiation with wavelength for different surface features before and after the normalization.

The mean value of the effective absorption cross-section (σ) was determined from ground-measured irradiance spectra for different sites using Eq. (1) assuming the CO_2 concentration obtained from Orbiting Carbon Observatory-2 database for the day of ground measurements and an altitude of 3 km for CO_2 column. Fig. 3 displays the spatial distribution of CO_2 obtained by applying the above algorithm to AVIRIS-NG images.

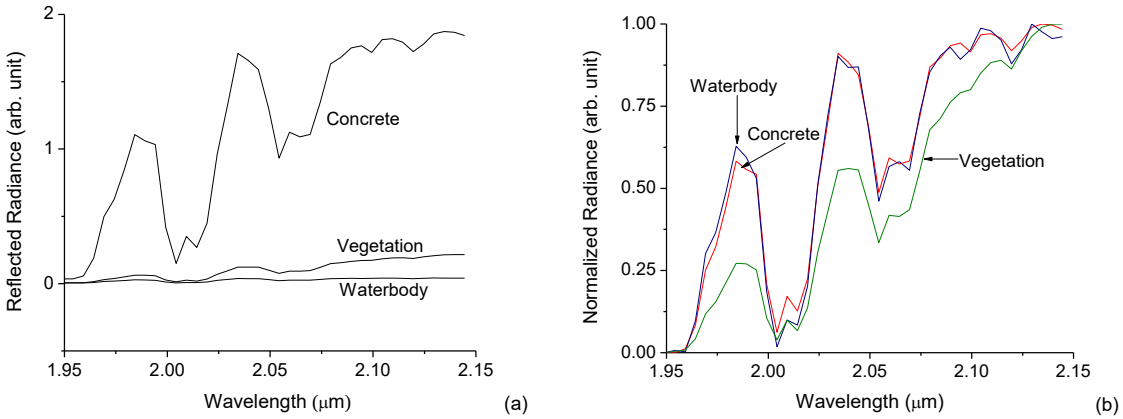

Fig. 2. Variation of reflected radiance with wavelength over the CO_2 absorption regions of different pixels for different surface features in AVIRIS-NG image: (a) original state, (b) after normalization with Eq. (4).

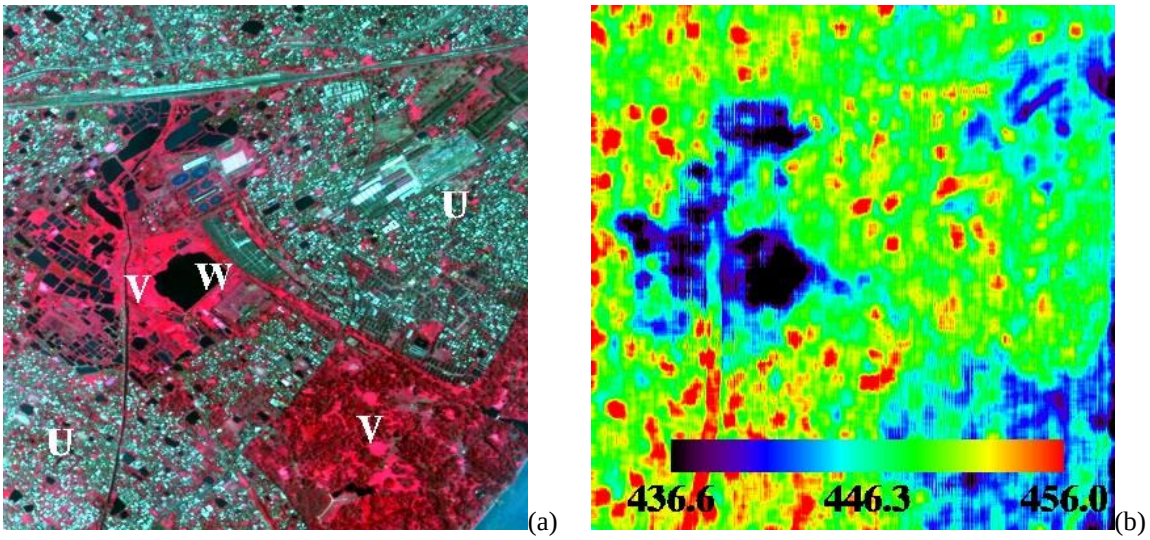

(a) (b)

Fig. 3. (a) A segment of AVIRIS-NG image containing distinct waterbody (W), vegetated region (V) and non-vegetated urban zone (U) and (b) the corresponding spatial distribution of CO_2 concentration (ppm).

2. Water Vapor Correction

The CO_2-1 absorption band is partly overlapped by the adjacent water vapor absorption band (Fig. 1), which is taken into account. Fig. 4(a) illustrates the gradual change of the absorption depths with water vapor concentration using model radiance spectra for tropical urban atmosphere under different conditions of atmospheric water vapor simulated with MODTRAN6 (Spectral Sciences Inc.) software. Many such spectral curves were generated and the radiance ratio (L_0/L_a) for CO_2-1 band was determined for each case. Fitting the ratios with the corresponding water vapor concentration (g cm^{-2}) values, the CO_2 concentration was determined. For water vapor concentration of around 2.8 g cm^{-2}, a value close to that during image procurement, the CO_2 concentration was found to be increased by about 9% with respect to the assumed value for simulation. The result is shown in Fig. 4(b).

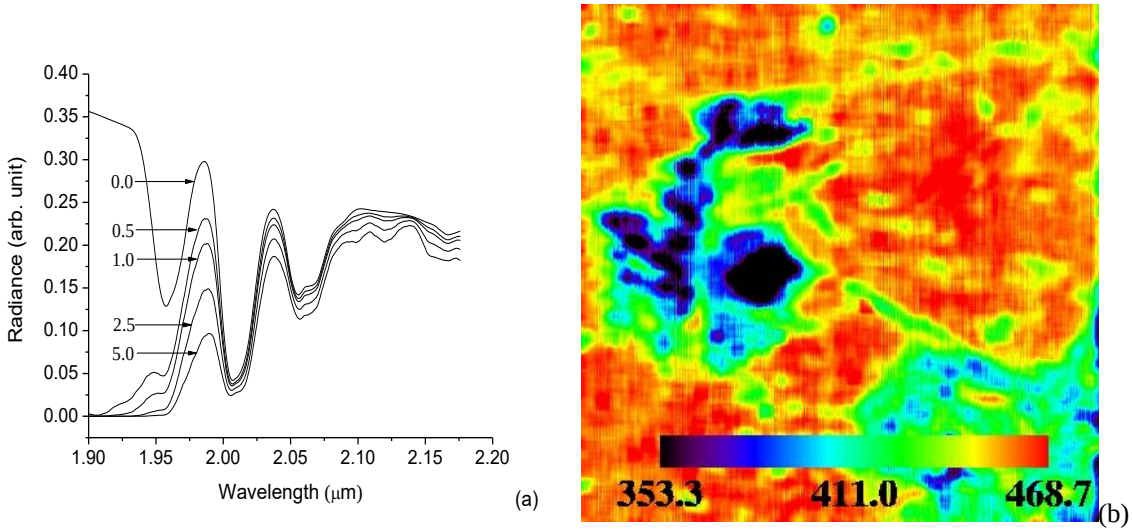

Fig. 4. (a) MODTRAN simulation of CO_2 absorption bands for tropical urban atmosphere with assumed CO_2 concentration of 400 ppm and different values of water vapor concentration (g cm^{-2}) indicated against the curves. (b) Spatial distribution of CO_2 concentration (ppm) estimated from CO_2-1 absorption band for the image of Fig. 3(a) using the same algorithm as earlier and including 9% increase for water vapor effect on the absorption depth.

Also, a new technique was proposed to get rid of the water vapor absorption effect by comparing with the spectral signature obtained from the atmosphere of the planet Mars, which is mostly composed by CO_2 at very low atmospheric pressure and can be used as a model. The images of Mars procured by Compact Reconnaissance Imaging Spectrometer for Mars (CRISM) covering 1.002–3.920 μm with resolution of 0.00655 μm per channel were downloaded (http://crism.jhuapl.edu/data/publicData.php) and the spectra were derived with ENVI+IDL v4.7 image processing software having CRISM Analysis Tool (CAT) v7.4 (https://pds-geosciences.wustl.edu/missions/mro/crism.htm) plugged in. To minimize the random error, a number of spectra were taken for random pixels from both AVIRIS-NG and CRISM images. A 'representative' spectrum of each category was created by the technique of singular value decomposition (SVD) Technique. Some results are given in Fig. 5.

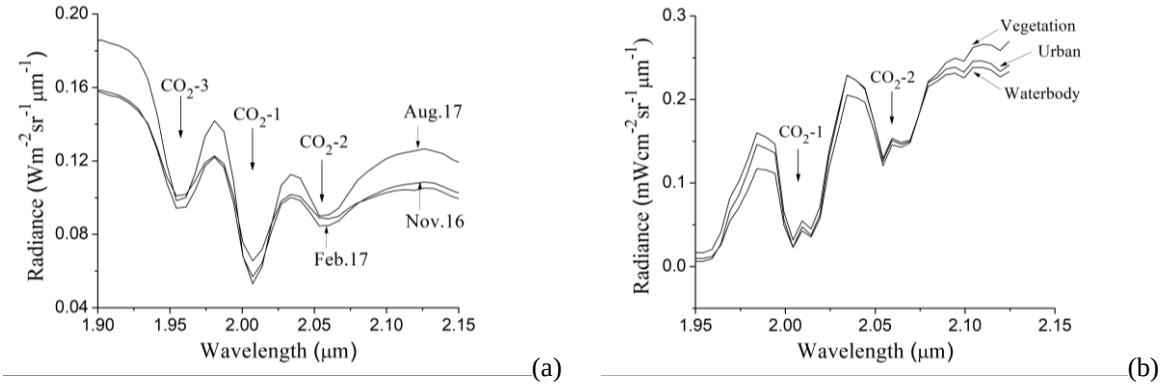

Fig. 5. (a) Radiance spectra for Mars derived from CRISM images of different seasons containing three CO_2 absorption bands designated as CO_2-1, CO_2-2 and CO_2-3, respectively. (b) Radiance spectra for earth's atmosphere derived from AVIRIS-NG images for vegetation, waterbody and urban regions. The CO_2-1 and CO_2-2 absorption bands are obtained.

Fig. 6 shows the radiance spectra simulated with MODTRAN6 code over large range of CO_2 and H_2O concentration, which exhibits that the terrestrial spectra gradually transform alike with the spectra of Mars for zero water vapor condition.

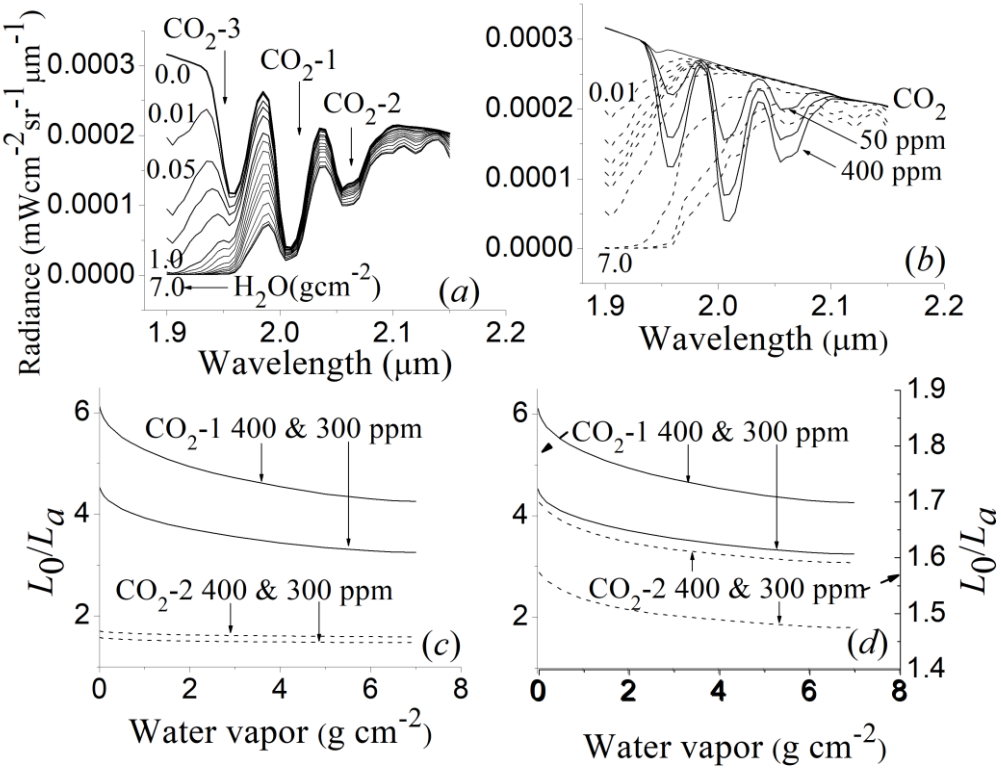

Fig. 6. Synthetic radiance spectra illustrating: (a) absorption due to different H_2O concentrations (g cm^{-2}) with CO_2 400 ppm, (b) overlapping of CO_2 absorption with zero H_2O (solid lines) and H_2O absorption with zero CO_2 (dotted lines), (c) radiance ratio (L_0/L_a) of CO_2-1 and CO_2-2 in the same scale and (d) in individual scales.

The H_2O absorption modifies both CO_2-1 and CO_2-2 depths [Fig. 6(b)] but CO_2-2 is much less affected, as apparent from their individual radiance ratios (L_0/L_a) in the same scale [Fig. 6(c)]. However, the trends of variation with H_2O concentration are the same for both the absorptions [Fig. 6(d)] so that their ratio would vary almost linearly for finite CO_2 concentrations. The above findings from terrestrial, Martian and synthetic spectra give the idea that the actual absorption depth of CO_2-1 band in absence of H_2O and its truncation in presence of H_2O can be correlated in terms of the ratio (R) of CO_2-1 and CO_2-2 absorption depths and the original CO_2-1 depth can be recovered from the experimentally obtained truncated depth in terms of R. Fig. 7 explains the process with the variation of R over large range of CO_2 and H_2O concentrations with two different surface features and infers that whatever CO_2-1 depth is obtained from the terrestrial spectra in presence of H_2O, can be multiplied by a constant term to obtain the corrected value. In the present case of CO_2 assessment from AVIRIS-NG images, an increase of 14% in the CO_2-1 absorption depth is found to be appropriate.

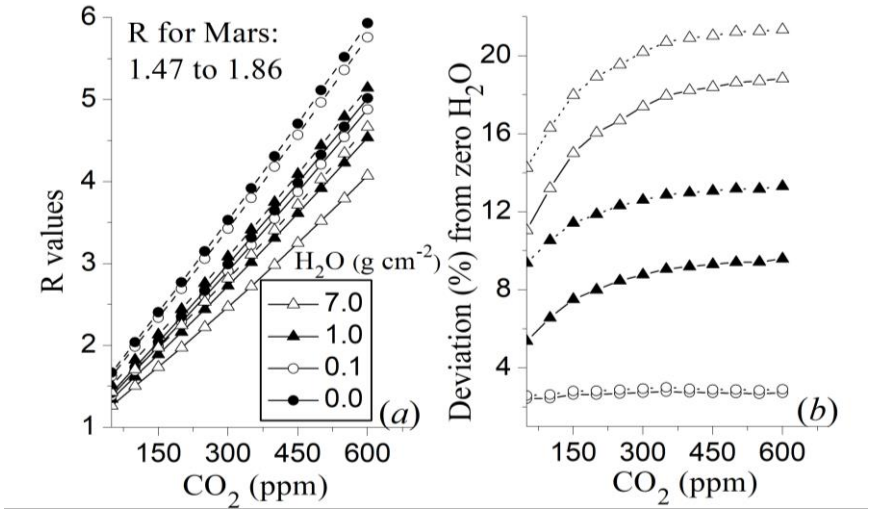

Fig. 7. (a) Variation of CO_2-1 to CO_2-2 absorption depth ratio (R) with CO_2 (ppm) and H_2O (g cm^{-2}) concentrations simulated for earth's tropical atmosphere with surface features: urban (solid line) and grassland (dashed line). (b) The corresponding percentage deviation in R from that with zero water vapor (symbols are same as those of Fig. 7(a).

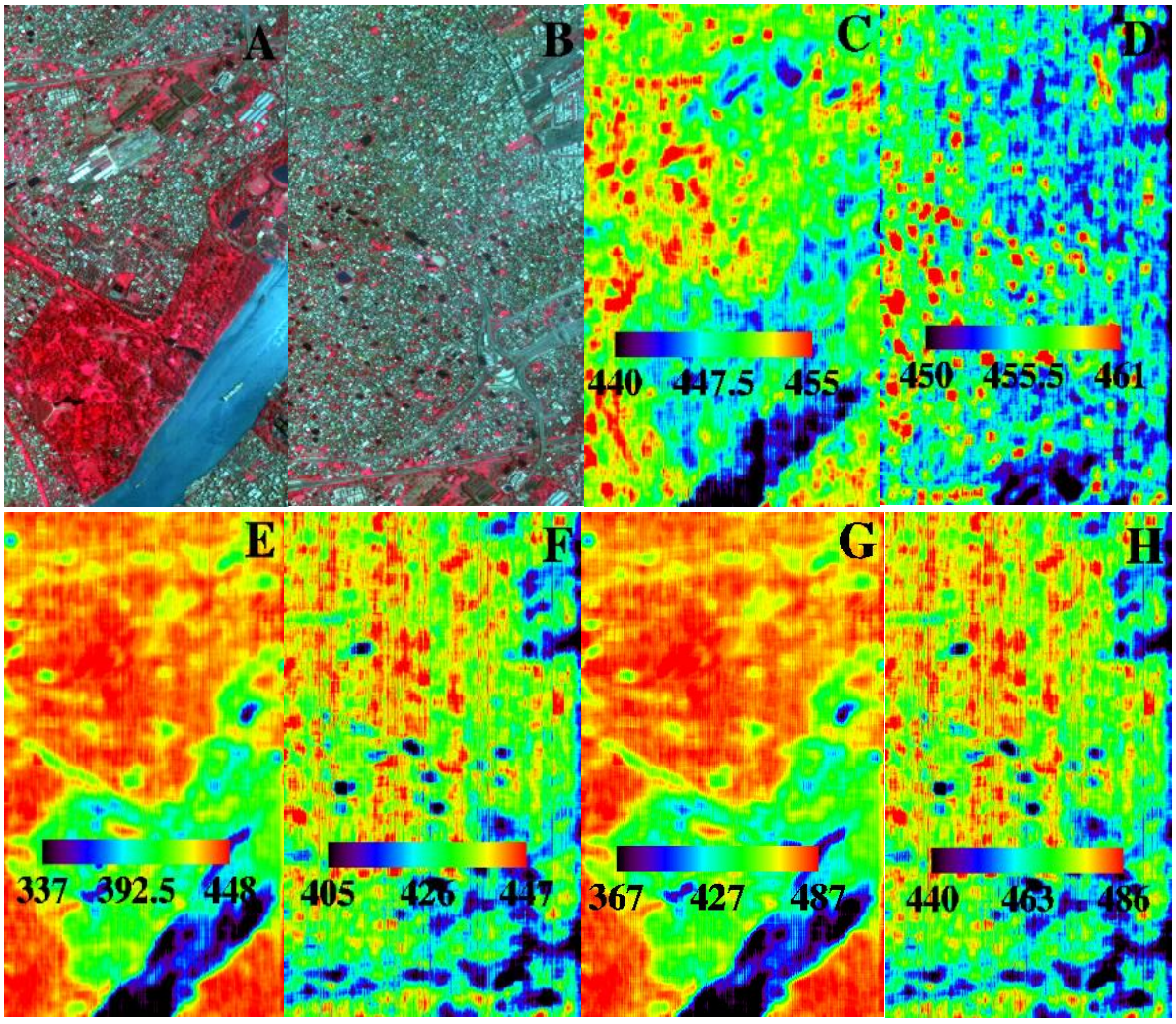

Fig. 8. (A) & (B) AVIRIS-NG image segment of densely populated area and corresponding CO_2 map (C) & (D) derived from CO_2-2 depth, (E) & (F) CO_2-1 depth and (G) & (H) CO_2-1 depth with H_2O correction.

Fig. 8 presents some examples of spatial distribution of CO_2 assessed from AVIRIS-NG images using the present methodology with and without H_2O correction. The CO_2 concentrations in Fig. 8 may be compared with concurrent ground-measured column average of 336–438 ppm estimated from ASD spectroradiometry and surface-level 386–542 ppm for places of varied urban congestion.

3. Detecting Point Sources of CO_2

The versatility of the spatial mapping from hyperspectral images is established by implementing this on AVIRIS-NG hyperspectral images of two different sites containing a coalfield, which is assumed to contain larger CO_2 concentration and adjacent urban area with general enhanced CO_2 level for increased human activities (Figs. 9 and 10).

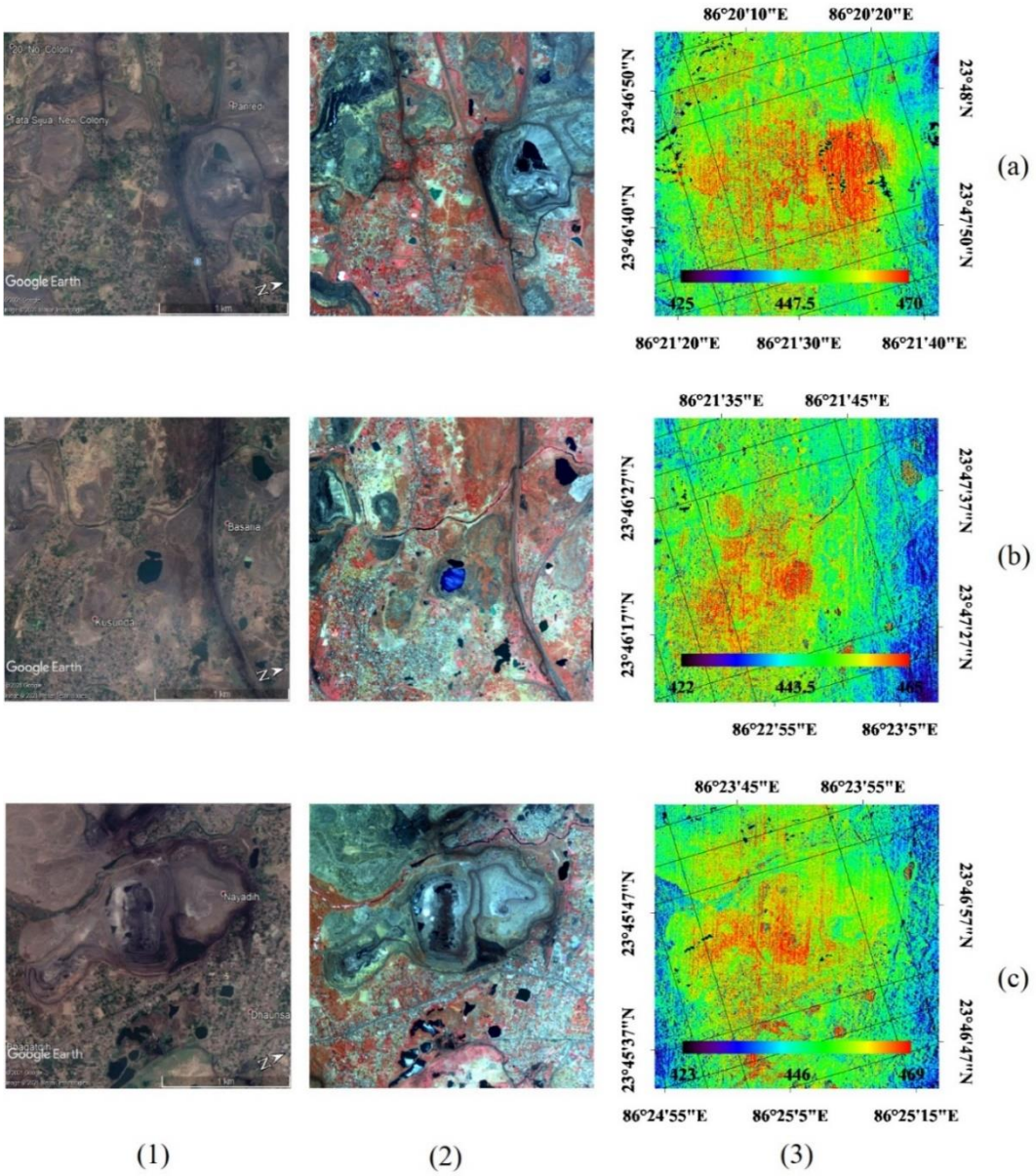

Fig. 9. Three different regions (a), (b) and (c) of the coal field area with (1) the corresponding google earth image, (2) the AVIRIS-NG false color image segment and (3) the corresponding spatial distribution of CO_2 concentration (ppm).

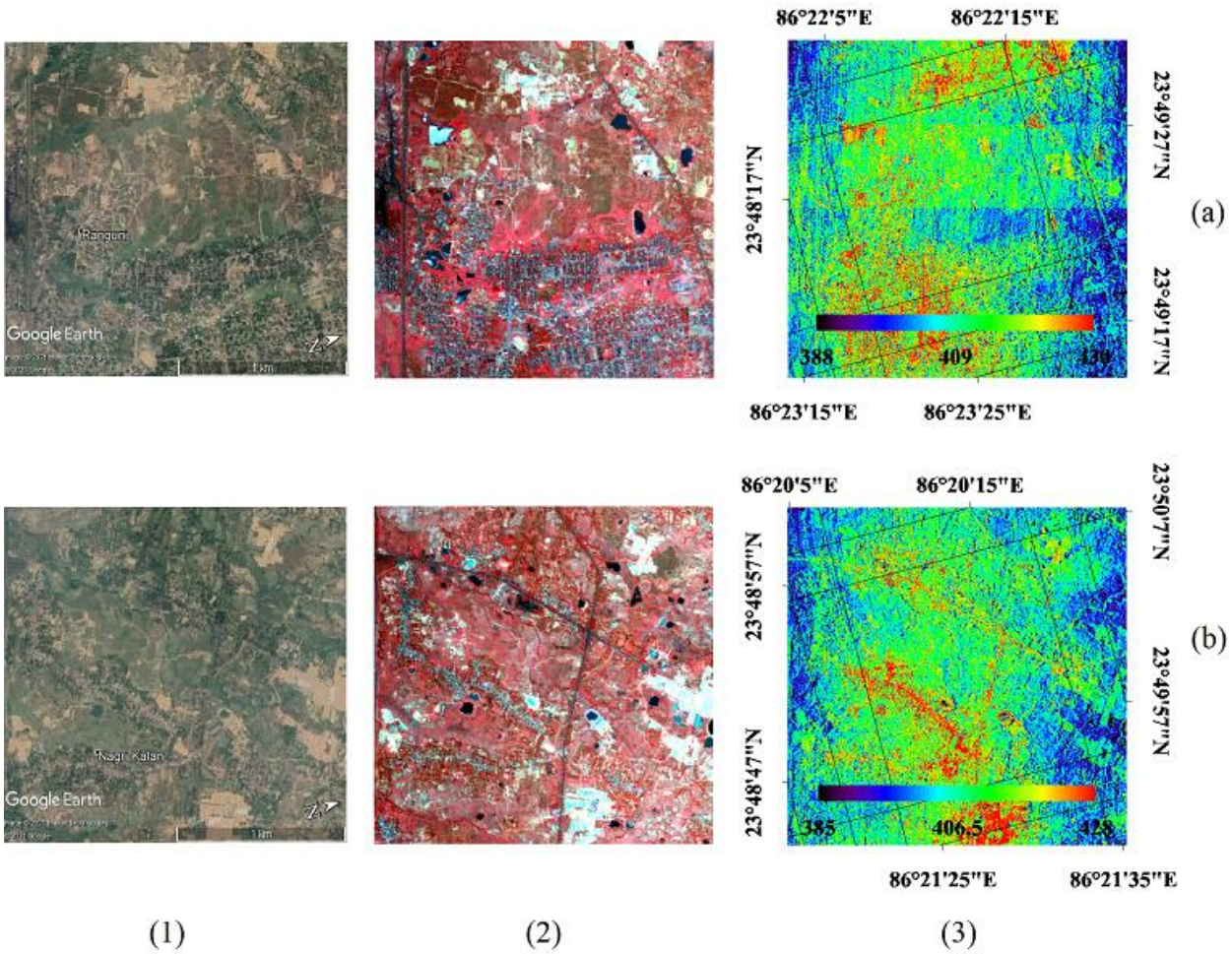

Fig. 10. Two different locations (a) and (b) of the surrounding urban area of the coalfield in Fig. 9 with (1) the corresponding google earth image, (2) the AVIRIS-NG false color image segment and (3) the corresponding spatial distribution of CO_2 concentration (ppm).

Three separate regions of the coal field area are displayed in Fig. 9. Distinctly higher values of CO_2 concentration are noted at the actual coal field areas, as understood from the AVIRIS-NG and Google Earth images. Fig. 10 consists of similar arrangement of images and CO_2 distributions for ordinary urban areas nearby the coal fields. Here the CO_2 concentration is not so localized but scattered over the whole area. Comparing the results of Fig. 9 and Fig. 10, it is apparent that the present method is capable of identifying point sources of CO_2 having localized enhancement.

The significance of a technique like the present one is further emphasized with Fig.11 that plots the available xCO_2 values in the year 2018 for the two regions each of 1°×1° span, one (23.2° N – 24.2° N, 85.8° E – 86.8° E) enclosing Jharia coal field and the other (21.8° N – 22.8° N, 87.7° E – 88.7° E) including urban areas of Kolkata and Howrah. It is interesting to note that the overall CO_2 concentrations of these two different regions remain confined within the same range of about 400 – 415 ppm whereas the concentration in the coal field area is much larger, about 425 – 470 ppm (Fig. 9). The presence of a significant CO_2 source is thus averaged out in the coarse spatial resolution (≈ 1 km × 2 km) of the global monitoring system. The detection of any specific local change calls for higher spatial resolution in the observation like the present one.

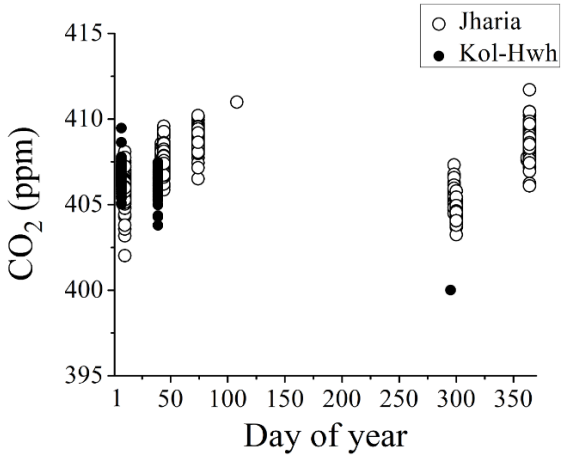

Fig. 11. The available xCO_2 values in the year 2018 for the regions enclosing the coal field (Jharia) and the Kolkata-Howrah urban areas.

4. CO_2 Seasonal Variability

The general trend of the temporal variation of atmospheric CO_2 concentration exhibits a continuous increase with time superimposed by an oscillatory seasonal change, the latter being ascribed to the seasonal change of vegetation vigour. However, other interesting features, such as sub-annual variation, El-Nino events and many other anomalies related to the CO_2 concentration are testified simultaneously. This work investigates the possible effect of atmospheric temperature and pressure on such seasonal changes by exploring the CO_2 data derived from Carbon Observatory-2 (OCO-2) and develops a mathematical model to explain the change of CO_2 concentration at an arbitrary altitude with respect to that at the ground surface due to change in temperature and pressure.

The number density of atmospheric CO_2 at an arbitrary altitude z is given by combination of two components as

$$N(z) = n(z) + \upsilon(z) \tag{5}$$

where the first term $n(z)$ depends only on air-pressure and the second term $\upsilon(z)$ depends on sources and sinks irrespective of air pressure and accounts for the vertical change of CO_2 mixing ratio due to the diffusion of surface air throughout the atmosphere.

Let n_1 and n_2 be the number densities of CO_2 molecules at the same altitude (z) for two different surface temperatures (T_{01} and T_{02}) and n_{01} and n_{02} be the corresponding ground level number densities. Let the CO_2 column reaches up to an altitude of z_1 when the ground level temperature is T_{01}. If this temperature is increased to T_{02}, the same number of CO_2 molecules attains an increased height of z_2 due to decrease in pressure and consequent expansion. The integrals of Eq. (5) over the altitude should be equal for these two cases because the total number of molecules throughout the atmospheric column is to remain the same. Therefore,

$$\int_0^{z_1}(n_1 + v)dz = \int_0^{z_2}(n_2 + v)dz \tag{6}$$

The changed number density at ground surface with change in temperature can be obtained as

$$n_{02} = n_{01}(T_{01}/T_{02})\,\frac{1-(1-\Gamma z_1/T_{01})^{k+1}}{1-(1-\Gamma z_2/T_{02})^{k+1}} \tag{7}$$

Eq. (7) put forward the concept that the seasonal change in surface air temperature can cause change in air pressure so that the expansion or contraction can give rise to an apparent change in the gas concentration at any specific altitude. It indicates that the path of radiation propagation through the CO_2 molecules becomes longer in comparison with that at lower temperature thereby raising the possibility of undergoing more absorption and yielding apparently higher value of concentration.

The annual variations of CO_2 at the specified region, as obtained for years 2016 and 2017 are displayed in Fig. 12. In order to understand the trend of seasonal variation, the plotted points were fitted with 3rd order polynomial. All the plots have the tendency of increasing CO_2 concentration in summer season.

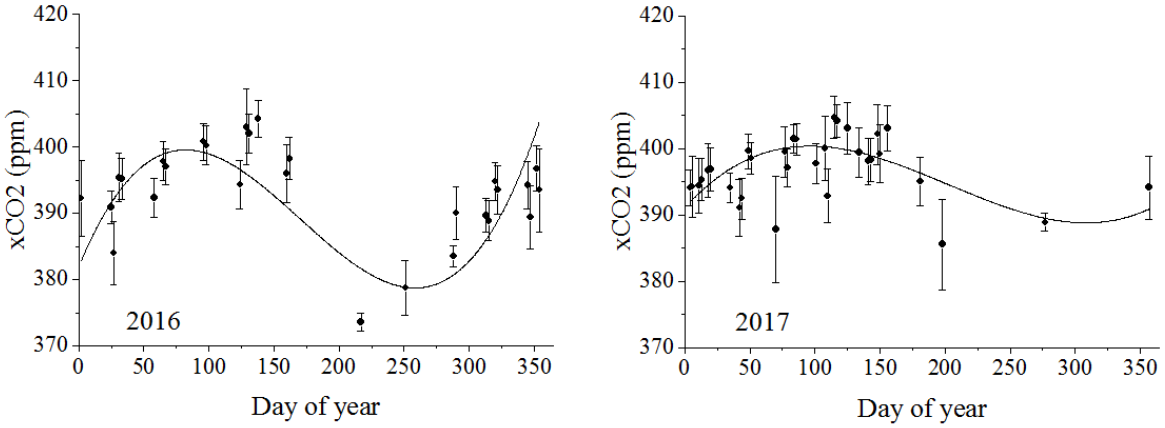

Fig. 12. Annual variation of xCO_2 (ppm) for years 2016 and 2017, extracted from OCO-2 database for the region within 22° N to 23° N and 86° E to 89° E.

Fig. 13 represents the seasonal change of the surface pressure extracted from OCO-2 database for the region and period mentioned in Fig. 12. The corresponding air temperatures obtained from the same data source are also plotted for comparison. It is apparent from Fig. 13. that the surface pressure decreases in monsoon and autumn seasons and increases in the winter (two ends of the year). The opposite trend is shown by the surface air temperature.

The Fourier transform in Fig. 14 establishes that the seasonal changes of both the NDVI and the atmospheric pressure are related to the seasonal change of CO_2 but none of these two is sufficient alone to explain the phenomena. The increasing phase of NDVI does not synchronize with the decreasing phase of CO_2 so that the carbon uptake period cannot be correlated directly with the vegetation dynamism. Similarly, the annual growth and decay of surface pressure does not coincide with that of CO_2 and there remains a difference of several months between them.

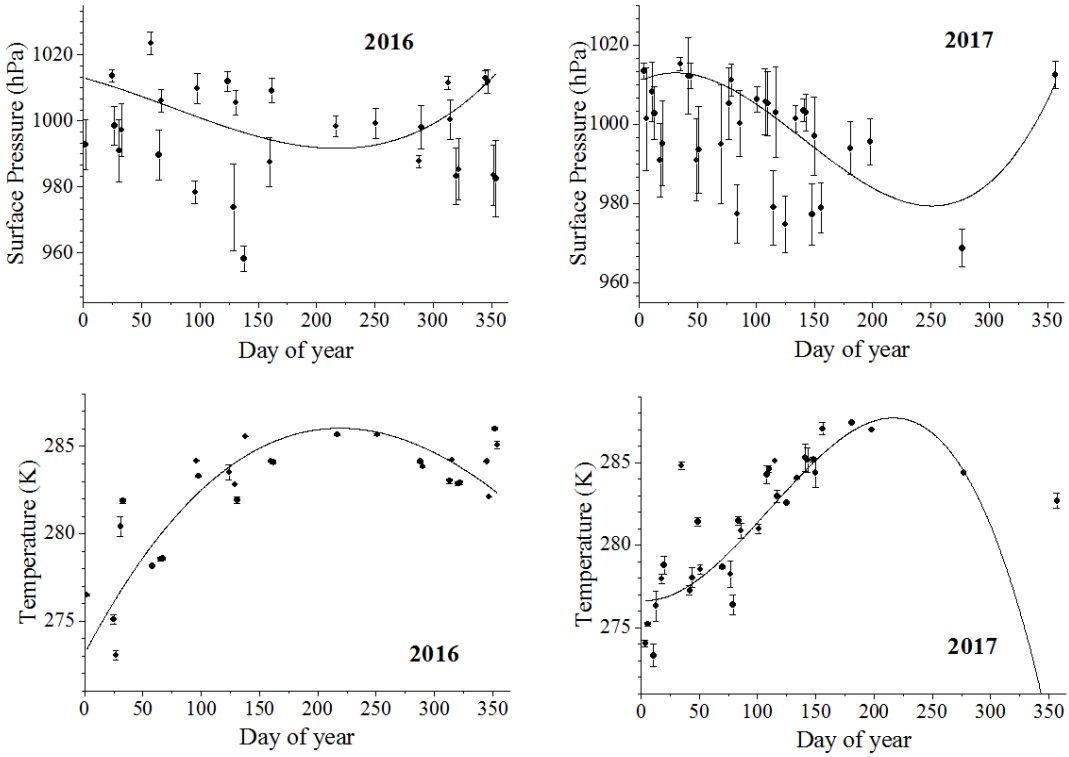

Fig. 13. Annual variation of surface pressure (hPa) and air temperature (K) for years 2016 and 2017, extracted from OCO-2 database for the region within 22° N to 23° N and 86° E to 89° E.

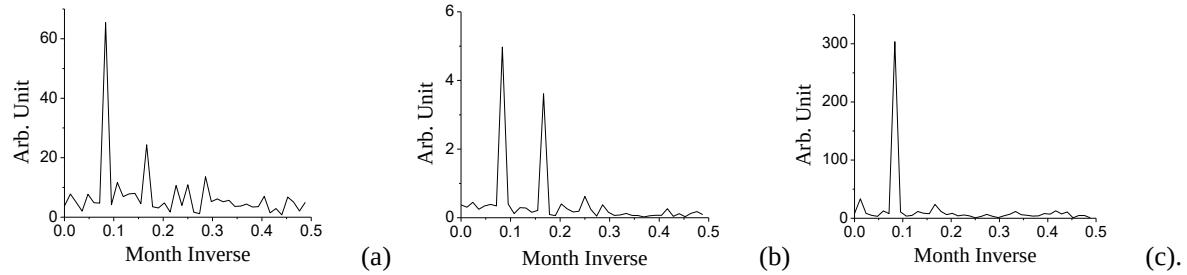

Fig. 14. Fourier transform for (a) CO_2, (b) NDVI and (c) surface pressure for the areas specified with Fig. 12.

As obvious from the above discussions, the periodic change in atmospheric pressure has significant role in causing the annual change in CO_2 concentration. A possible reason of such phenomenon may be the transfer of more surface-level CO_2 to higher altitudes thereby increasing the effective concentration through the whole atmospheric path for the solar radiation. A theoretical model for the above idea, is given in Fig. 15. It indicates that the change in air temperature changes the air pressure in such a way that the CO_2 concentration at ground-level decreases and that at higher altitude increases. Thus, the CO_2 vertical concentration profile gets changed irrespective of the presence of the vertical transport component.

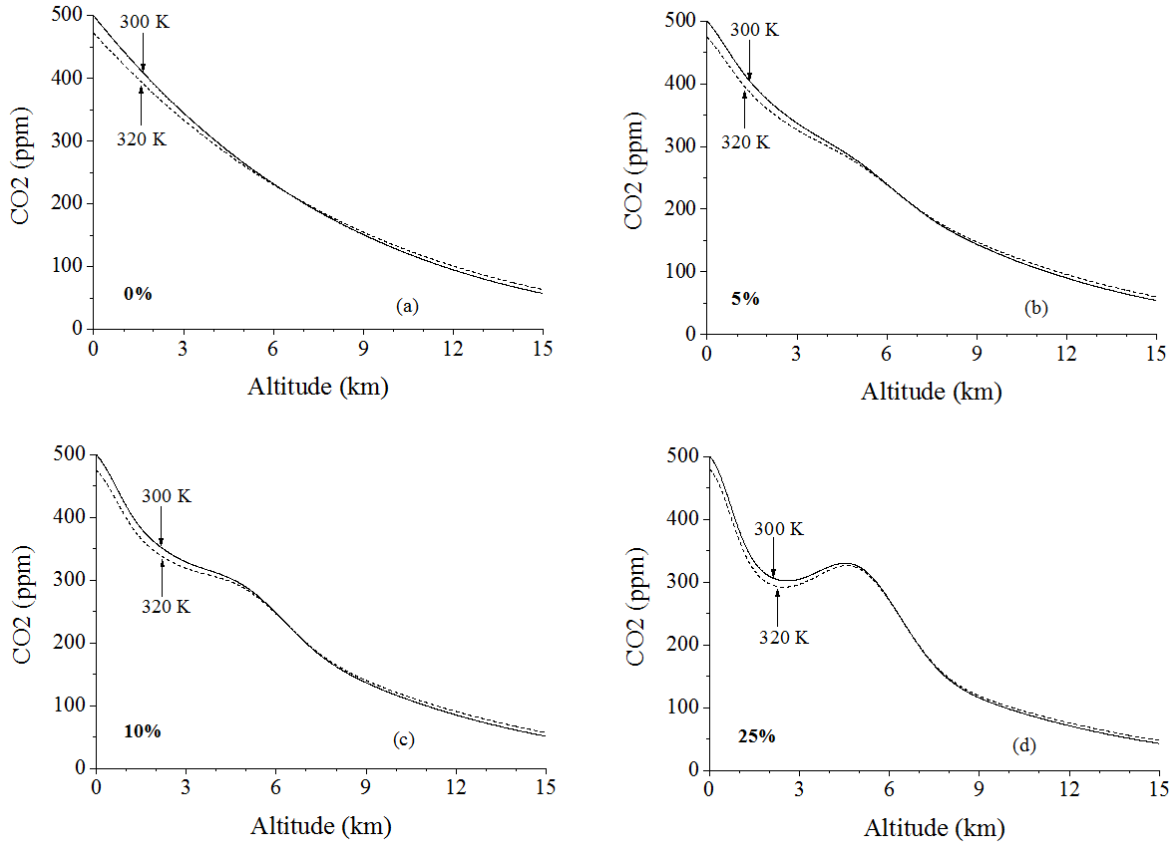

Fig. 15. Theoretical curves for CO_2 vertical concentration profile generated with Eq. (5), (6) and (7) indicating the change in air temperature causing change the air pressure such that the concentration decreases at ground level and increases at higher altitudes in presence of vertical transport component of (a) 0%, (b) 5%, (c) 10% and (d) 25%. Parameters: a = 5 km, w = 2 km.

5. Assessment of Recent Global CO_2 Scenario

Orbiting Carbon Observatory-2 or OCO-2 and Orbiting Carbon Observatory-3 or OCO-3 are two dedicated ultra-spectral carbon sensors with possession of 0.1 nm spectral resolution. OCO-2 is established for last 7 years, mounted on a sun-synchronous A-train satellite constellation becoming the 6th satellite in the group, orbiting almost 705 km above earth surface. OCO-3 is the most recent CO_2 sensor, a newer version of OCO-2 and mounted on the International Space Station at approximately 410 km altitude. It is recording data since August 2019 to the present day.

The main goal for this work was to explore the seasonal change of CO_2 derived from the new global CO_2 sensor OCO-3. Accidently an unexpected constraint situation of the global pandemic due to Novel Corona Virus in 2019 (COVID-19) came into effect, restricting normal human activities. There is a possibility that this restriction could somehow affect the carbon emission due to reduced fossil fuel burning. That motivated the way of work for the investigation of CO_2 reduction for restricted human activity.

To validate this change at global level, many urban and nine urban and uninhabited places (with negligible human activity) were verified for having uniformly distributed data throughout the year and ultimately nine places of each category, each of 2°×2° latitude-longitude span were chosen from all over the world.

A comparison between the former OCO-2 and newer OCO-3 is checked with suitable polynomial fit of 3 years of data of 2018, 2019 and 2020. In Fig. 16. (a) all 3 years of carbon dioxide data were procured from OCO-2 and in Fig. 19. (b) OCO-2 data for 2020 was replaced with OCO-3 data for the whole year of 2020. This OCO-2 and OCO-3 case is used to compare those above-mentioned sensors.

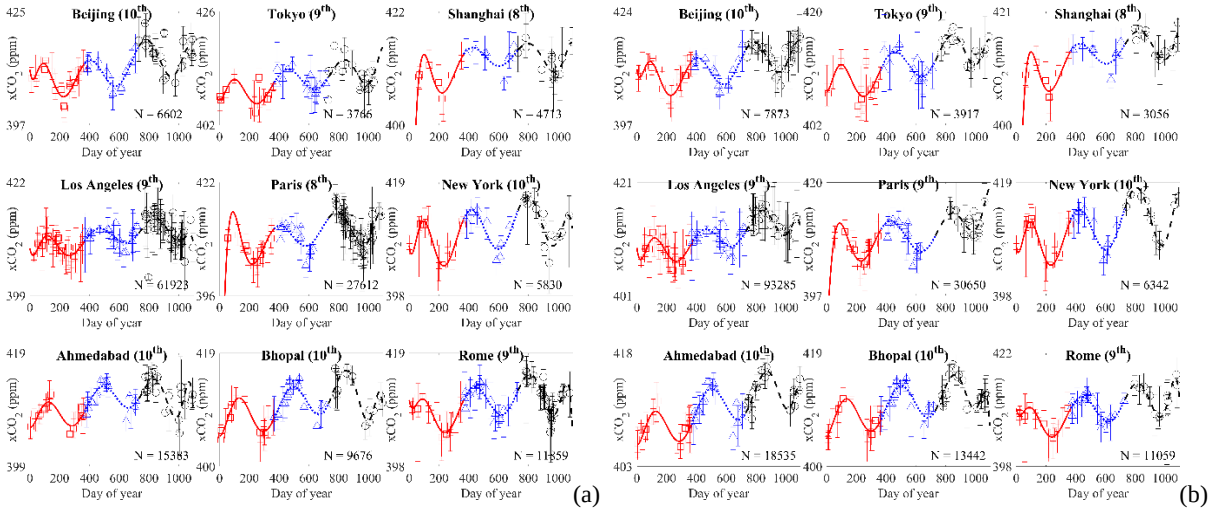

Fig. 16. Seasonal variations of xCO_2 from year 2018 to 2020 for the nine urban places (Table 3), derived from (a) all OCO-2 (left) and (ii) OCO-2, 2018 & 19 with OCO-3, 2020 (right). Symbol & fitting line: 2018 ≡ square & red-solid, 2019 ≡ triangle & blue-dotted and 2020 ≡ circle & black-dashed. (N = number of good data points found in 3 years span.)

The goodness of fit for n days or the minimization of residual error was decided by Bayesian information criterion (BIC) given by

$$BIC = n \ln\left[\frac{1}{n}\sum_{i=1}^{n}(y_i - \hat{y}_i)^2\right] + k \ln(n) \quad (8)$$

where y_i and $\hat{y}_i$ are the actual and the fitted value, respectively, for the i^{th} data point. The k corresponding to the minimum BIC value was considered as the polynomial order for fitting. The fitted orders for all the nine urban places around the world for both OCO-2 and OCO-3 case lies within 8^{th} to 10^{th} order, which was expected. In order to quantify the observational inferences on the annual xCO_2 variation for each region, two parameters were defined in relation to the fitted curves. One was named 'drop time', denoting the number of days between the xCO_2 extrema and the other was the ratio of the maximum-minimum xCO_2 difference to the corresponding difference of days, designated as 'slope'.

Both OCO-2 and OCO-3 have gone through the period of the global shutdown and the corresponding decrease in fossil fuel emissions in 2020.

Fig. 17. Comparison of the drop time (day) and the slope (ppm/day) for the xCO_2 annual variations obtained from OCO-2, 2018 to 2020 (upper panels) and OCO-2, 2019 & 20 and OCO-3, 2020 (lower panels) for all the urban regions of Fig. 19.

Fig. 17 compares the drop time (day) and the slope (ppm/day) for the xCO_2 annual variations obtained from OCO-2, 2018 to 2020 (upper panels) and OCO-2, 2019 & 20 and OCO-3, 2020 (lower panels) for all the urban regions of Fig. 16. It is interesting to note that in almost all the cases, the slope has increased in 2020 with respect to 2019, both for OCO-2 and OCO-3. This is just opposite to the natural trend of xCO_2 change from 2018 to 2019. The drop time also exhibits opposite results for 18-19 and 19-20. These results imply that the xCO_2 in year 2020 started to drop down earlier and began to rise again later than that in the previous years.

Fig. 18 represents the xCO_2 variations in the places free from human activity, derived from OCO-2 and OCO-3 and plotted in the same manner as that of Fig. 16. Mixed results are obtained for these regions. The reverse xCO_2 trend for the locations of the Southern hemisphere may also be noted. As a whole, the deviation of xCO_2 in year 2020 is much less prominent in the remote, unpopulated regions.

The above observations infer that the abrupt reduction in worldwide human activity of fossil fuel burning during the last year have been reflected globally, strongly or weakly at different places, in the atmospheric CO_2 column average. The situation has distorted the normally anticipated seasonal variation of xCO_2 and has raised the necessity of quantifying the deviance from the actual trend of CO_2 variation obtainable from OCO-3. The wavelet analysis is put forward for that purpose using the OCO-2 data of 2019 as the reference.

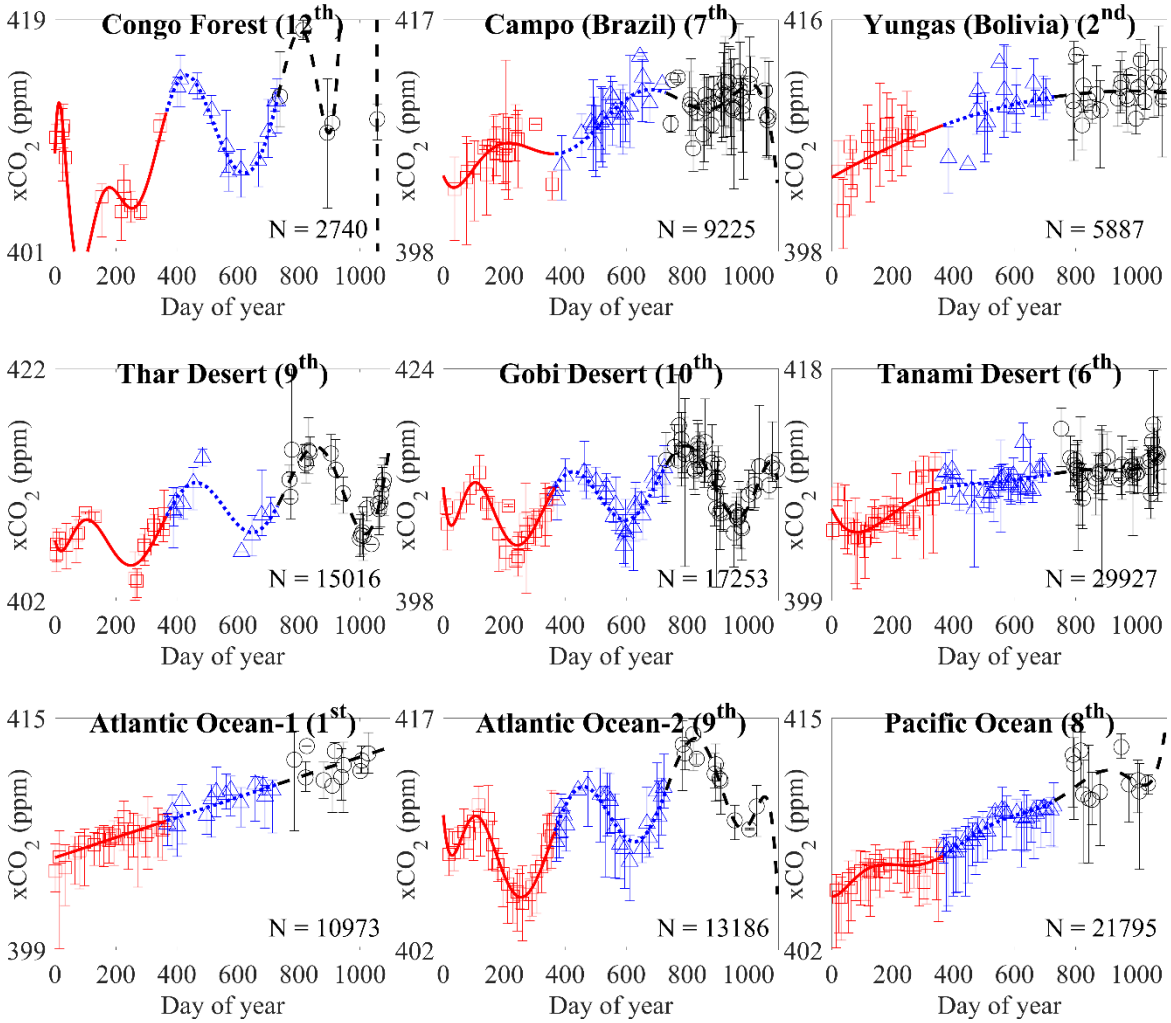

Fig. 18. Seasonal variations of xCO_2 from year 2018 to 2020 for the nine unpopulated places, derived from OCO-2, 2018 & 19 and OCO-3, 2020. Symbol & fitting line: same as Fig. 16.

Wavelet cross spectrum is a fine tool to study the localized changes of two, time variables. In our case the variables would be the xCO_2 value of 2109 and 2020. With this technique any similarity or dissimilarity can be pointed out easily. In order to estimate the deviation with respect to the usual seasonal variation, the annual xCO_2 obtained from OCO-2 for the year 2019, cut out from the Fig. 16. (b) was taken as the reference and wavelet coherence was executed with similarly cut out annual xCO_2 obtained from OCO-3 in the year 2020.

Each region was tested independently for any localized phase consistency. Fig. 19 shows one such example (Los Angeles). The major portion of the plot, as understood from the color bar, indicates almost total coherency of the xCO_2 of both the years (OCO-2, 2019 and OCO-3, 2020) for the whole period. The corresponding phase arrows depict the matrix of phase angles between the same for those two years. Some localized phase differences take place within the triangular mid-region (white shaded) with both time and frequency, as indicated by the phase arrows.

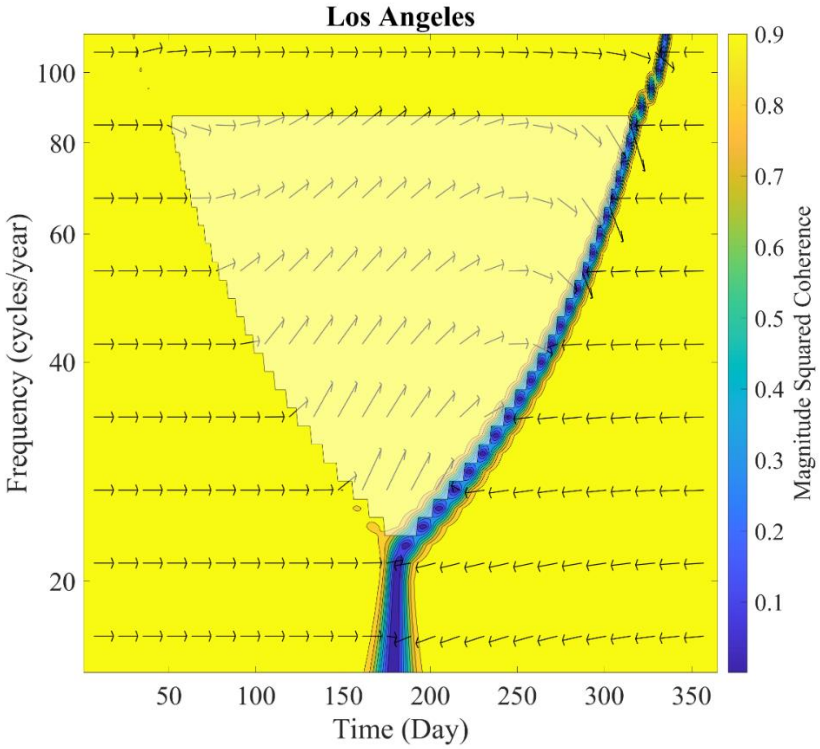

Fig. 19. An example (Los Angeles) of wavelet coherence of the xCO_2 annual variation obtained from OCO-2, 2019 and OCO-3, 2020.

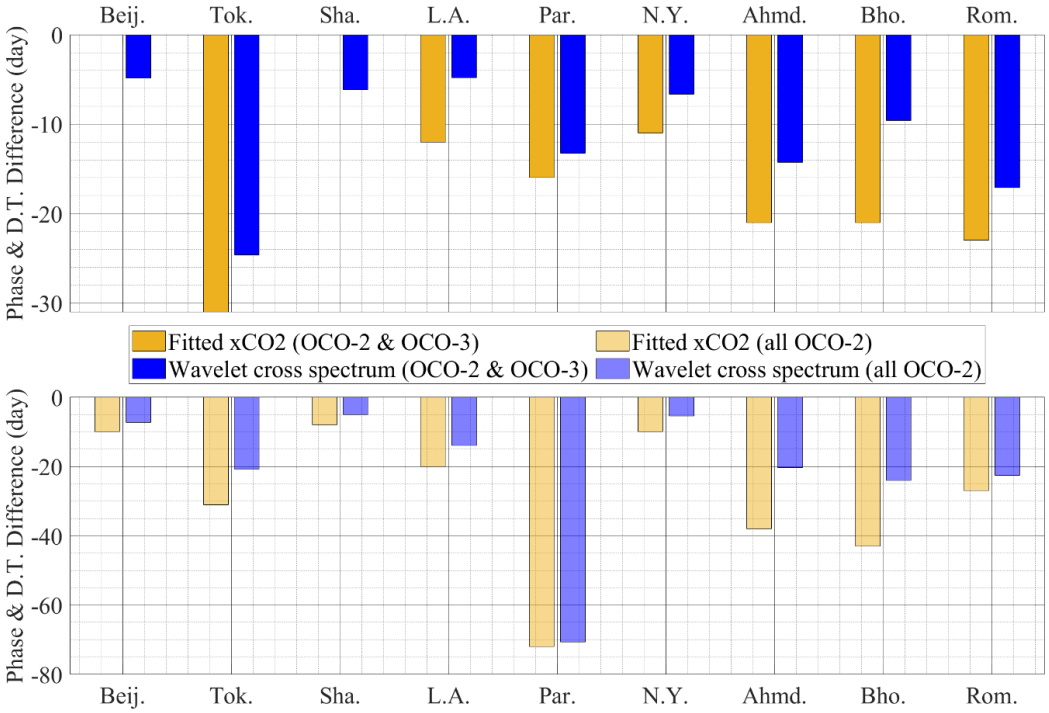

Fig. 20. Comparison of the wavelet phase difference and the difference in drop time of the fitted xCO_2 curves of (i) OCO-2, 2019 and OCO-3 2020 (top) and (ii) OCO-2, 2019 and OCO-2 2020 (bottom) for the urban places abbreviated in the same sequence as that given in Fig. 17.

To compare this Drop time difference or Phase Spread acquired from wavelet technique with the actual Drop time difference calculated from the Fitted graphs are showed in Fig. 20.

It presents a concrete estimate of the phase differences for all the urban areas and compare those with the drop time difference obtained from the fitted xCO_2 curves for the urban places (abbreviated) in the same sequence as that given in Fig. 17. It is found from Fig. 20 that the span of phase change obtained from wavelet coherence is well consistent with the drop time difference of the fitted curve. Therefore, one can estimate the phase difference of the annual xCO_2 variation derived from OCO-3, 2020 as a measure of deviation with respect to the variation obtained at normal situation, the OCO-2, 2019 being used as the proxy at present. This work thus demonstrates the wavelet coherence technique as a tool for quantifying the unexpected deviation from the usual annual xCO_2 variation obtained from OCO-3 database using the corresponding OCO-2 data as reference. In future, a similar methodology can be executed with the own data of OCO-3 procured in tentatively normal situations.

6. Estimating Aerosol Concentration

The optical depth is an important parameter in connection with the spatial distribution, particulate concentration and size estimation of aerosols, which is estimated with Beer-Bouguer-Lambert law using the information on the transmission of radiation of some specific wavelengths through the atmosphere with less attenuation. The extraterrestrial radiation at the top of the atmosphere is needed as a reference. The present work has put forward a simple method for estimating the aerosol optical depth using the O_2-A band. It is different from the earlier studies as it employs two non-absorbing band, instead of one, on either side of the absorbing band. No reference parameter like top-of-atmosphere reflectance is needed.

For any arbitrary wavelength, the radiance (L_m) measured at the sensor is the algebraic sum of the source radiance (L_s) emitted from the source or reflected from the object surface, atmospheric gaseous absorption, if any, and path radiance (L_p) acquired due to scattering from aerosols and Rayleigh scattering. For the NIR wavelength range (750–775 nm) around O_2-A band, Rayleigh scattering is negligible and only the aerosol contribution is significant. The measured radiance at the wavelength of maximum absorption within O_2-A band can be expressed as

$$L_{ma} = TL_s + L_{pa} \tag{9}$$

T is the atmospheric transmittance in this band. The subscript 'a' stands for 'absorption'. For any other non-absorbing wavelength outside this band, the measured radiance is

$$L_m = L_s + L_p \tag{10}$$

Here T becomes unity (100%) because of no specific gaseous absorption. If, instead of a single wavelength, several reference wavelengths are used, (16) can be generalized as

$$T = \frac{L_{ma} - L_{pa}}{\sum_i w_i (L_{mi} - L_{pi})} \tag{11}$$

Here w_i is the relative weight of the i-th band. For each wavelength pair λ_1 and λ_2 on either side of the absorbing wavelength λ_a, the weights are expressed as

$$w_1 = \frac{\lambda_2 - \lambda_a}{\lambda_2 - \lambda_1} \quad \text{and} \quad w_2 = \frac{\lambda_a - \lambda_1}{\lambda_2 - \lambda_1} \tag{12}$$

The atmospheric path radiance within O_2-A band may or may not be equal to that outside the band. In either case, the former can be expressed as a fraction or multiple of the later so that

$$L_{pi} = q_i L_{pa} \tag{13}$$

q_i being a constant of proportionality for the *i*-th band. Using Eq. (13) in (11) and rearranging one can obtain a relative optical depth for the gaseous absorption as

$$T_0 = T + \frac{L_{pa}}{\sum_i w_i L_{mi}}(1 - T\sum_i w_i q_i) \quad (14)$$

$T_0 = \frac{L_{ma}}{\sum_i w_i L_{mi}}$ is the experimentally measurable relative optical depth of O_2-A band in presence of aerosols. Eq. (14) includes the contribution of both oxygen absorption and aerosol scattering. Putting $L_{pa} = 0$ in Eq. (14) makes $T_0 = T$ indicating that in absence of any aerosol, the relative optical depth corresponds to the transmittance in O_2-A band is solely due to the gaseous absorption. It is termed 'relative' because the absorption is estimated with respect to the measured spectral data itself. No absolute reference, such as the extraterrestrial radiation is considered for the radiation passing through the atmosphere.

Fig. 21 compares the spectral variation of the optical depth determined from the present measurements with the standard results obtained from several nearest available AERONET sites, both being based on Beer-Bouguer-Lambert law. It is noted that the absolute values change widely but the nature of variation remains the same as that of Fig. 21(a), which justifies that the relative change in irradiance values with wavelengths can produce similar information on optical depth as that obtained from absolute values. This concept is applied in the present methodology.

Fig. 22 generates different theoretical values of optical depth using Eq. (14) changing q_i and L_{pa} parameters. The aerosol path radiance values are assigned as different percentages of the measured radiance (L_{ma}) within O_2-A band; zero percent being the state of no aerosol. It is noted that even with much exaggerated values of q_i, the transmittance does not reduce by more than 17%. Therefore, it is not unjustified to assume $q_1 = q_2 = 1$ meaning the same path radiance throughout the wavelength range under consideration.

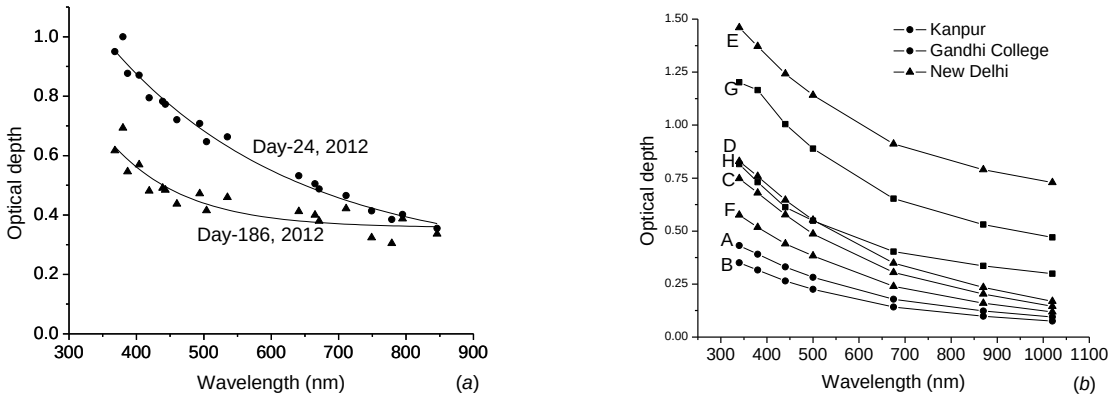

Fig. 21. Comparison of optical depth values obtained from (a) present measurements (22°39´19.24" N, 88°23´00.33" E) and (b) AERONET sites: Kanpur (26°30´46" N, 80°13´55" E), Gandhi College (25°52´15" N, 84°07´40" E) and New Delhi (28°37´48" N, 77°10´30" E) for different days of different years indicated against the curves as follows: A=Day-24,2012; B=Day-25,2012; C=Day-25,2012; D=Day-27,2012; E=Day-183,2011; F=Day-188,2011; G=Day-184,2009; H=Day-187,2009.

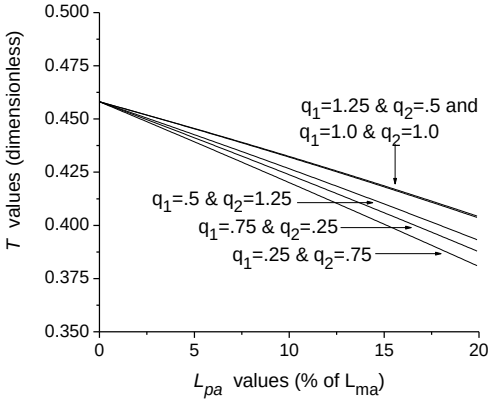

Fig. 22. Theoretical variation of relative optical depth within O_2-A band (760 nm) generated with Eq. (14) for different percentages of aerosol path radiance (L_{pa}) and relative contributions of two reference wavelengths (756 nm and 772 nm) to path radiance defined by q_1 and q_2, respectively.

The proposed technique is validated with two Hyperion images of densely populated urban areas of Kolkata for two different years and seasons, as shown in Fig. 23(a) and (b) where the spatial variation of relative optical depth (T_0) [Eq. (14)] is estimated with the relevant bands, namely band-41 (762.6 nm) corresponding to oxygen absorption and bands 40 (752.4 nm) and 42 (772.8 nm) used reference wavebands. Both the images display densely populated urban area with isolated vegetated regions 'A' and 'B'. Regions 'C' and 'D' are parts of river [Fig. 23(a)] and inland waterbody [Fig. 23(b)]. The spatial variation of the optical depths obtained from these two images, as calculated from Eq. (14) are shown in Fig. 24(a) and (b), respectively.

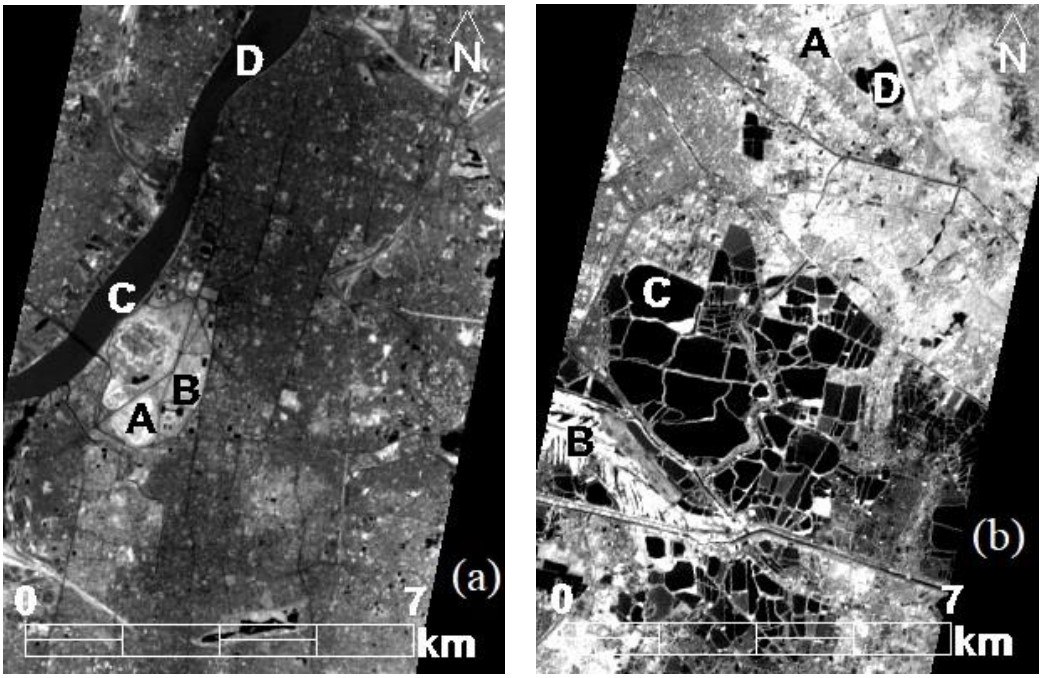

Fig. 23. Hyperion images of Kolkata dated (a) July 27, 2002 and (b) January 6, 2010 showing vegetated zones 'A' & 'B' and waterbody 'C' & 'D'

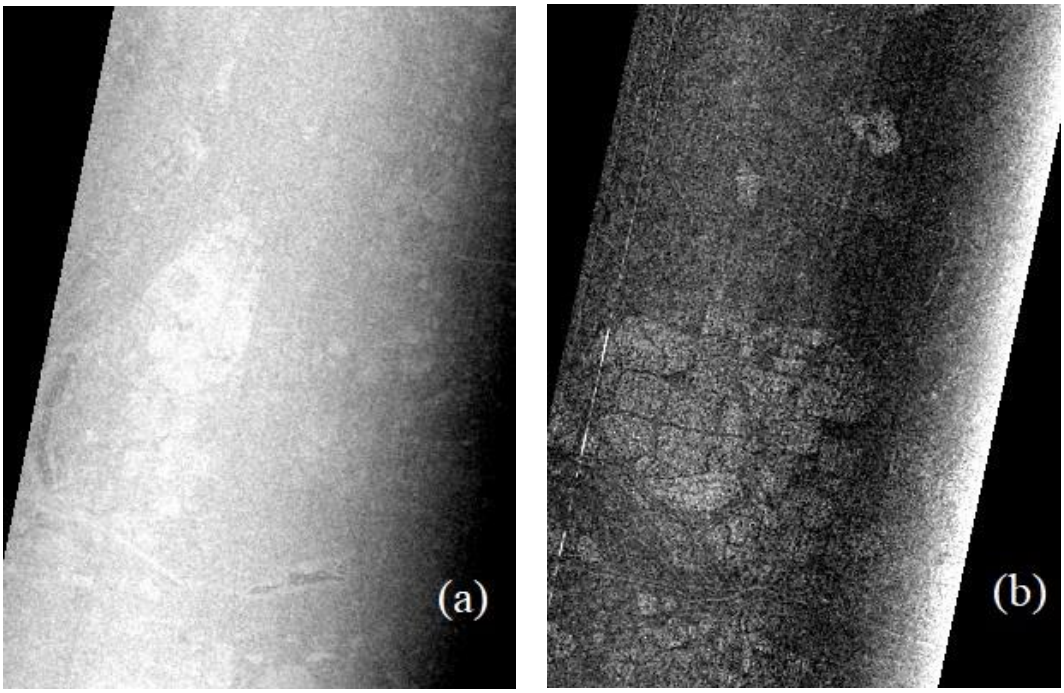

Fig. 24. Spatial variation of relative optical depth due to aerosol obtained from (a) Fig. 23(a), 0.95 to 1.02 and (b) Fig. 23(b), 0.64 to 0.69.

Typically, aerosol optical depth is calculated with the bands where no other absorption is present, but this work showed that using the absorption band is also a good choice.

7. Conclusion

The present work is motivated by the seriousness of atmospheric greenhouse gas monitoring and has chosen atmospheric CO_2, the most significant anthropogenic greenhouse gas for the study. Another accompanying parameter of human activity, namely urban aerosol is also taken into account. Spectroscopic analyses are carried out at different levels for estimating the atmospheric CO_2 and aerosol. Rigorous ground measurements on hyperspectral spectroscopy were conducted around the urban areas of Kolkata and Howrah. Airborne (AVIRIS-NG) and satellite (Hyperion) hyperspectral images were procured for these areas and spectral data for CO_2 absorption were derived from it and compared with ground truth. New methodologies are developed for estimating the spatial distribution of CO_2 (named *a*-DOAS) and aerosol (from O_2-A absorption) from hyperspectral image analysis. The huge database of the recent dedicated CO_2 sensors, namely OCO-2 and OCO-3 are explored in detail both at local and global level and several models are developed for (i) the seasonal change of CO_2, (ii) the vertical redistribution of CO_2 and the correction for the water vapour absorption effect on the CO_2 absorption band. The contemporary seasonal variations of the aerosol optical depth were also tracked. In course of the studies, it is detected that the sudden global lockdown occurred recently due to pandemic situation has reduced the atmospheric column average of CO_2 and a wavelet analysis technique is put forward to assess the extent of such deviation from the normal situation. As a whole, the work has attempted the level best to develop further the current concepts on anthropogenic CO_2 monitoring both from theoretical and experimental points of view.

List of Publications

Journal Papers

1. Barun Raychaudhuri and Santanu Roy (2020) "Martian atmospheric spectral radiance used as model for water vapor correction of terrestrial carbon dioxide absorption profile around 2 μm." *IEEE Geoscience and Remote Sensing Letters*, doi: 10.1109/LGRS.2020.3007378.
2. Barun Raychaudhuri and Santanu Roy (2020) "Investigation of seasonal variability of atmospheric columnar CO2 over India in relation to environmental parameters using OCO-2 observation and vertical redistribution model." *International Journal of Remote Sensing*, 42(4), 1450–1473, doi: 10.1080/01431161.2020.1832281.
3. Barun Raychaudhuri and Santanu Roy (2021), "A proof of concept for estimating the annual atmospheric carbon dioxide variation from Orbiting Carbon Observatory-3 vEarly data." *IEEE, Geoscience and Remote Sensing Letters*, doi: 10.1109/LGRS.2021.3099172.

International Conference Papers

1. Santanu Roy and Barun Raychaudhuri, "Detection of point source of carbon dioxide using hyperspectral imaging sensor." *IEEE CONECCT 2021.* (Presented by Santanu Roy)
2. Barun Raychaudhuri and Santanu Roy, "Retrieval of aerosol parameters from the oxygen absorption band of Hyperion hyperspectral image validated with spectroradiometry." *URSI Asia-Pacific Radio Science Conference 2019, New Delhi, India, 09–15 March 2019.* (Presented by Santanu Roy)
3. Barun Raychaudhuri, Sasmita Chaurasia, Santanu Roy, "Spatial variation of atmospheric carbon dioxide concentration retrieved from AVIRIS-NG images including water vapor correction and spectroradiometric validation for two urban places of India." *Proc. SPIE 11152, Remote Sensing of Clouds and the Atmosphere XXIV, 111520E (9 October 2019);* doi: 10.1117/12.2532027. *Event: SPIE Remote Sensing, 2019, Strasbourg, France*. (Presented by Prof. Barun Raychaudhuri)